Proceedings of ASME Turbo Expo 2011
GT2011
June 6-10, 2011, Vancouver, British Columbia, Canada

GT2011-46420

COMBUSTOR DESIGN OPTIMISATION USING CO-KRIGING OF STEADY AND UNSTEADY TURBULENT COMBUSTION

Moresh J. Wankhede*
University of Southampton
Southampton, United Kingdom

Neil W. Bressloff
University of Southampton
Southampton, United Kingdom

Andy J. Keane
University of Southampton
Southampton, United Kingdom

ABSTRACT

In the gas turbine industry, computational fluid dynamics (CFD) simulations are often used to predict and visualize the complex reacting flow dynamics, combustion environment and emissions performance of a combustor at the design stage. Given the complexity involved in obtaining accurate flow predictions and due to the expensive nature of simulations, conventional techniques for CFD based combustor design optimisation are often ruled out, primarily due to the limits on available computing resources and time. The design optimisation process normally requires a large number of analyses of the objective and constraint functions which necessitates a careful selection of fast, reliable and efficient computational methods for the CFD analysis and the optimization process. In this study, given a fixed computational budget, an assessment of a co-Kriging based optimisation strategy against a standard Kriging based optimisation strategy is presented for the design of a 2D combustor using steady and unsteady Reynolds-averaged Navier Stokes (RANS) formulation. Within the fixed computational budget, using a steady RANS formulation, the Kriging strategy successfully captures the underlying response, however with unsteady RANS the Kriging strategy fails to capture the underlying response due to the existence of a high level of noise. The co-Kriging strategy is then applied to two design problems, one using two levels of grid resolutions in a steady RANS formulation and the other using steady and unsteady RANS formulations on the same grid resolution. With the co-Kriging strategy, the multi-fidelity analysis is expected to find an optimum design in comparatively less time than that required using the high-fidelity model alone since less high-fidelity function calls should be required. However, using the applied computational setup for co-Kriging, the Kriging strategy beats the co-Kriging strategy under the steady RANS formulation whereas under the unsteady RANS formulation, the high level of noise stalls the co-Kriging optimisation process.

1. INTRODUCTION

In the early days of gas turbine combustor design, the design methodology typically involved using a number of empirical relations in combination with semi-empirical techniques supported by experiments [1, 2]. The design optimisation procedure was largely trial-and-error based where the method was to continually test different variants of the combustor until a suitable arrangement was found. In order to reach a good design this approach was costly and time-consuming [3]. Due to advances in computing power and development of CFD codes, combustor design and development processes have changed significantly, and CFD has now become a valuable part of an overall integrated combustor design system [4]. However, for combustor design optimisation the use of CFD has yet to overcome some obstacles in terms of combustion modelling accuracy and validation. It is well-known that an aero-engine gas turbine combustor is a complex aero-thermal system, consisting of a turbulent reactive flow-field together with multiple time-dependent physical-chemical processes, which occur at varying time and length scales [5]. Furthermore, the comprehensive physics implied by turbulent reacting flows involves strongly coupled behaviour between flow-field dynamics and combustion mixing processes. Hence, CFD simulation of a gas turbine combustor, embracing many complex thermal/fluid dynamic phenomena, presents an extremely challenging task requiring very fine spatial and

* Corresponding Author: Moresh.Wankhede@soton.ac.uk

temporal resolution of the computational domain and therefore very high computational expense [6].

Currently, combustor design and development strategies are being made more systematic and efficient using automated design tools, numerical analysis techniques and engineering know-how. At the design and concept development stage, computational fluid dynamics (CFD) simulations are often used to predict and visualize the reacting fluid dynamics, combustion mixing environment and emissions performance of a combustor [7]. Given the complexity in obtaining accurate flow predictions and due to the expensive nature of simulations, conventional techniques for CFD based combustor design optimisation are often ruled out, primarily due to the limits on available computing resources and time [8]. Additionally, the design optimisation process typically requires a large number of analyses of the objective and constraint functions. This necessitates a careful selection of fast, reliable and efficient computational methods for the optimization process. Currently, CFD-based design optimisation tools are mostly available for pure aerodynamic design problems [9]. The first attempt to introduce optimisation tools to aerodynamic design is associated with Lighthill [10]. More complicated and expensive CFD driven optimisation methods have appeared subsequently [11-13]. Recently, implementation of such optimisation tools to 3D aerodynamic problems has also been realized with success [14, 15]. However this advancement of CFD based optimisation tools has so far had a very limited impact on the field of combustor design optimisation. This is due to the fact that the complexity and associated cost of simulating combustion environments constrains the number of high-fidelity simulations that can be performed within limited computational time. Hence, a methodology that allows for rapid design optimisation with limited number of high-fidelity CFD analyses is required. For this reason, surrogate-model based optimisation methodologies have been proposed [16].

Surrogate-based design optimisation techniques including Kriging models have been used previously [17, 18] to accelerate the combustor design optimisation process by reducing the total number of high-fidelity CFD analyses. Jeong et al. [19] demonstrated, the possible approach of Kriging surrogate-model based optimisation strategy for a real-world combustion engineering application. It utilized a Kriging surrogate-model based optimisation strategy to optimize a diesel engine combustion chamber geometry. A 95% reduction in computational time was reported when using the Kriging strategy as compared to a direct search strategy with an evolutionary algorithm. Similarly, Duchaine et al. [20] presented a preliminary study of the feasibility of a fully automated decision-making tool for real aeronautical combustor optimisation again using a Kriging strategy. This approach proved to be feasible with the available computing power. Hence, it is now acknowledged that the Kriging model based optimisation strategy can, for certain combustor design problems, yield optimum designs within manageable timeframe by reducing the total number of high-fidelity CFD analyses that are needed. However, successful optimisation still largely depends on the total number of optimisation variables, objective and constraint functions and computational resolution used for each CFD analysis.

In this study, an assessment of a co-Kriging based design optimisation strategy (CKDOS) is presented for the design of a lean burn combustor using steady and unsteady RANS analysis of the turbulent combustion. This approach provides a way to achieve high-fidelity design optimisation at even more reduced cost (compared to traditional Kriging meta-model based strategies [19, 20]) by using a more accurate high-fidelity model in combination with a less accurate lower fidelity model (that is significantly less expensive to evaluate), both models being defined over the same design space. Here, a standard Kriging based design optimisation strategy is applied to design a two-dimensional lean burn combustion chamber using steady and unsteady RANS CFD analysis. Then, a co-Kriging strategy is applied using either two levels of grid resolutions in steady RANS formulation or using steady and unsteady RANS formulations on the same grid resolution.

2. COMPUTATIONAL MODEL

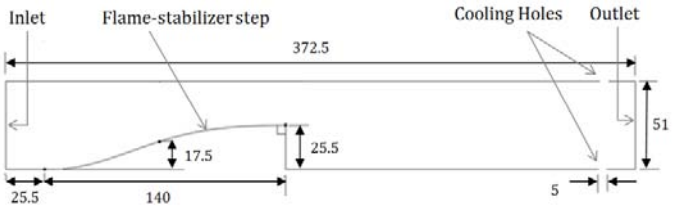

Fig. 1. Computational domain of the combustor with a flame-stabilizer step (All dimensions in mm)

The elementary interaction between a vortex and flame often represents a key process in the description of turbulent reactive flows [21]. Consequently, the combustor modeled for this design optimisation study is the one used by Keller et al. [22] in an experimental study of mechanisms of instabilities in turbulent combustion leading to flashback. The combustion chamber has an oblong rectangular cross section to model the essential features of planar flow and was provided with a profiled backward-facing step acting as the flame holder. Figure 1 shows the complete computational domain used for steady and unsteady RANS CFD analysis, indicating locations where inlet and outlet boundary conditions are specified. Important factors considered in the design of this combustion system by Keller et al. [22] were thorough mixing of propane and air before entering the test section and uniform velocity (flat inlet velocity profile) at the entrance to the test section (i.e. combustion chamber). Considering the experimental setup of Keller et al. [22], the premixing tube is not included in the computational model. Instead, the configuration (c.f. Figure 1) uses appropriate boundary conditions at the inlet and outlet of

the system. Additionally, cooling is provided near the outlet, both at the upper and the lower wall, of the combustor. The width of the cooling hole is 5 mm and is at a distance of 22mm from the outlet of the combustor. The combustion processes take place in the combustor at atmospheric pressure and hot gases including products exit from the outlet.

2.1 Boundary conditions

Table 1. Key CFD analysis parameters for Ansys Fluent 12.1	
Solver:	Pressure based
Turbulence model:	k - ε (standard)
Transport and reaction:	
Species	Partially premixed combustion
Mixture properties	PDF-mixture (propane + air)
Equivalence ratio	0.86
Boundary conditions:	
Inlet	Velocity-inlet
Inlet (Momentum)	For steady RANS; V_{in} = 13.3 m/s
	For unsteady RANS; User defined function with forced sinusoidal fluctuation at inlet, with frequency = 175 Hz and amplitude = 50% of inlet velocity V_{in} = 13.3 + 6.65*sin(1099.55*t) *(t = time-step size)*
Inlet (Temperature)	300 K
Outlet	Outflow
Cooling inlet	Velocity inlet; V_{in} = 13.3 m/s
Operating pressure:	101325 Pa
Convergence criteria:	1e-06 (for residuals of continuity, x-velocity and y-velocity)

Appropriate inlet and outlet boundary conditions are necessary for the simulation of instability processes [23]. To explore the flame/vortex dynamics in the combustor in an unsteady turbulent flow, a sinusoidal function (Table 1) is imposed at the inlet velocity boundary condition. This technique is indeed an easy way to represent the effect of an acoustic resonance in the reaction region [24]. The amplitude of the forcing fluctuation is 50% at a frequency of 175 Hz, which corresponds to the frequency of the humming cycle as reported by Keller et al [22]. Table 1 lists some of the key CFD parameters employed in the commercial CFD package Ansys Fluent™ version 12.1.The solver used is pressure based and has a second order implicit unsteady formulation for time. The standard k - ε model is used for turbulence modeling, with standard wall functions in Fluent™. The SIMPLEC pressure-correction method is used for pressure-velocity coupling. The combustion takes place at a lean equivalence ratio of 0.86. Fluent's partially premixed combustion model is used as the species model. The model solves a transport equation for the mean reaction progress variable $\bar{C}$, (to determine the position of the flame front), as well as the mean mixture fraction $\bar{f}$, and the mixture fraction variance $\overline{f'^2}$. Ahead of the flame ($\bar{C}$ = 0), the fuel and oxidizer are mixed but unburnt, and behind the flame ($\bar{C}$ = 1), the mixture is burnt [25].

2.2 Mesh sensitivity study

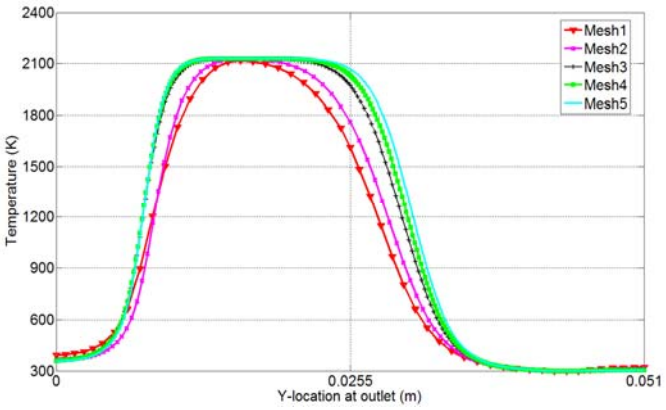

Fig. 2. Outlet temperature profiles as captured by different mesh sizes using steady RANS

Table 2. Mesh size and steady RANS analysis details			
Mesh	~ Cell count	~ Run-time (mins)	No. of iterations for solution
1	11000	10	1000
2	46000	30	4500
3	190000	210	13000
4	420000	1080	28000
5	800000	2400	40000

For determining the effect of mesh size on the CFD solution for the configuration shown in Figure 1, five multi-block structured meshes of increasing cell counts were constructed using GAMBIT™ version 2.3. A Y+ value of ~30 is maintained for meshes 1 and 2, where for meshes 3, 4 and 5 the Y+ value is less than five as a result of the finer resolution. Table 2 lists the cell counts of all meshes along with the computation time and iterations required to evaluate a converged reactive steady RANS solution using eight processes in parallel on a cluster using Intel quad core processors with 2.8GHz clock rate. Figure 2 shows the comparison between the predictions obtained from the five different meshes (c.f. Table 2) in terms of temperature profiles at the outlet plane of the combustor (c.f. Figure 1). As seen in Figure 2, the agreement between meshes is good near the walls of the combustor. Away from the walls, grid independence is approached by mesh 3, though it is not 100 % conclusive near the centerline of the combustor. Due to the significant increase in the computational expense produced by refining the mesh further (c.f. Table 2)

and from an engineering point of view of design optimisation, mesh 3 is deemed suitable for further CFD analysis and design optimisation. The solution obtained using mesh 1 is used as the low-fidelity solution for the co-Kriging optimisation strategy.

2.3 Time-step size sensitivity study

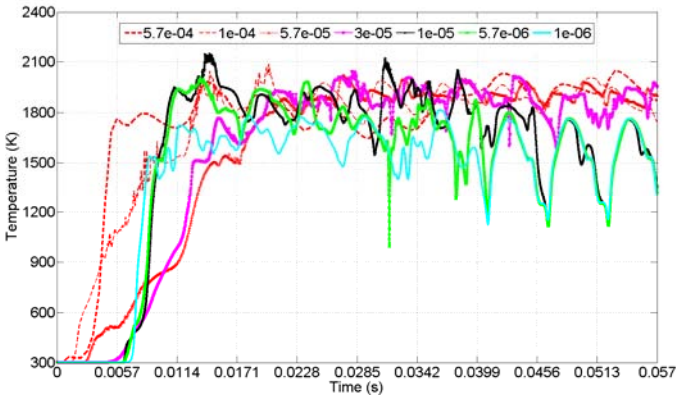

Fig. 3. Area-weighted average temperature (T_a) fluctuations at the outlet as captured by different time-step size URANS simulations

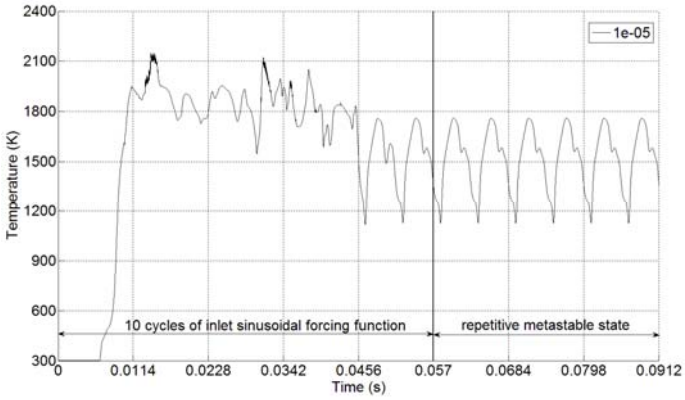

Fig. 4. Reactive flowfield settlement into meta-stable state as captured by time-step size 1e-05 URANS simulation

After investigating the effect of different mesh sizes on the outlet temperature profile using steady RANS, the combustor with cooling holes (c.f. Figure 1) is investigated using URANS on mesh 3, with the sinusoidal velocity variation at the inlet. The URANS simulation is run using different time-step sizes for 10 cycles of the sinusoidal forcing function in order to understand the effect of simulation time-step sizes on the average outlet temperature prediction patterns. Figure 3 shows the variation of area-weighted average temperature (T_a), as captured by different time-step size URANS simulations, at the outlet of the combustor. The coarser time-step size simulations are not able to capture the humming instability cycle in the reactive flow-field. The coarsest time-step size at which the URANS simulation successfully captures the humming cycle is 1e-05s. As shown in Figure 4, after the initial transient, the flow-field settles in to a repetitive cycle of temperature fluctuations by the end of ninth inlet velocity cycle, with a peak temperature value of ~ 1800K and minimum of ~ 1200 K. The URANS simulation is further run with finer time-step sizes of 5.7e-06s and 1e-06s, and these results agree closely with the simulation results for 1e-05s in the tenth cycle. Thus, the average outlet temperature variation predicted by URANS become independent of the simulation time-step size at 1e-05s, as further refining the simulation time-step size does not change the results significantly. Hence, a simulation time-step size of 1e-05s is used for further URANS analysis.

3. COMBUSTOR FLOWFIELD ANALYSIS

In steady RANS analysis, the flame front stabilization mechanism and the regions of burnt/unburnt mixture is of primary interest. In contrast, the unsteady RANS analysis is dominated by flame dynamical response to flow perturbations upstream. The objective here is to establish a suitable description of combustion and flame propagation in the combustor rather than to compute the reactive flow in all its complexity. Hence, a two-dimensional approach is used for the purpose of reproducing the basic features of the reactive flow downstream of the flame stabilizer step (c.f. Figure 1) including the recirculation zone, flame – recirculation zone interaction and the flame-front wrinkling process.

3.1 Steady RANS analysis

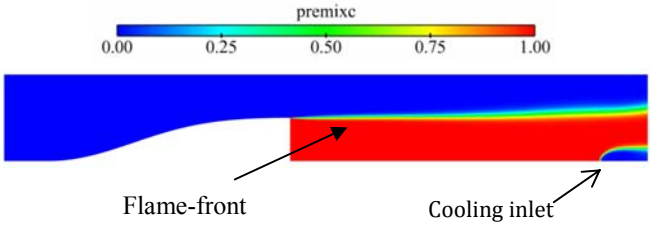

Fig. 5. Position of the flame front inside the combustor as captured by steady RANS

Statistically, steady turbulent flames require flame stabilization mechanisms [26]. The recirculation zone behind the step provides the low-speed region necessary for flame stabilization. Figure 5 shows the position of the flame front inside the combustion chamber, for the baseline design used for the optimisation study. As the Reynolds number of the flow is in the turbulent regime, the mixture burns only in the location where the turbulent flame speed S_T is able to sustain the mixture velocity $\tilde{u}$, i.e. the region behind the step. Therefore the chamber behind the step is separated into unburnt and burnt mixture regions by an interface, where combustion has started but not yet fully established. Above this surface ($\bar{C} = 0$), the fuel and oxidizer mixture is mixed but unburnt, and below this surface ($\bar{C} = 1$), the mixture is completely burnt [25].

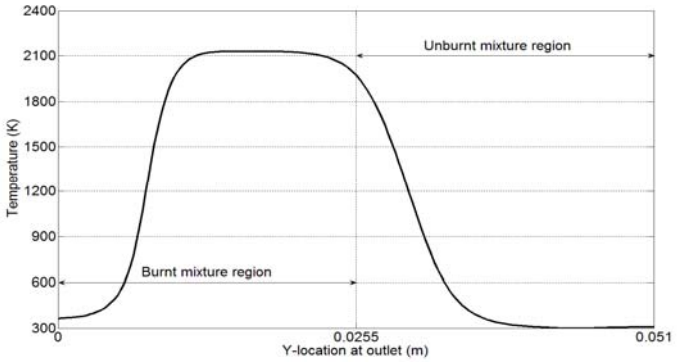

Fig. 6. Outlet temperature profile of the combustor (steady RANS)

Thus, due to a high mixture velocity in the upper part of the chamber behind the step, much of the mixture escapes unburnt from the combustor. Figure 6 shows the temperature profile at the outlet of the combustor. Due to the entrance of cooling air through the holes, near the outlet, the burnt mixture convecting downstream from the step interacts with the cooling air and flows over it. Thus, the outlet temperature in the burnt mixture region near the lower wall of the combustor is low, and rises significantly away from the lower wall (c.f. Figure 6). The temperature is maximum (~2100 K) in the burnt mixture region, reduces in the interface region and is lowest in the unburnt mixture region. The temperature of the mixture which escapes unburnt from the combustor remains at the inlet temperature level of 300 K.

3.2 Unsteady RANS analysis

Flame-vortex dynamics behind a backward-facing step has been examined experimentally and numerically previously. However, definitive conclusions regarding the flame-vortex dynamics have not yet been reached [27-29]. In most cases, it has been observed that under unstable operating conditions, as determined by the mixture equivalence ratio and Reynolds number, one or more large vortices periodically convolute the flame front during part of the instability cycle which leads to oscillations in the heat release rate. In a study by Ghoniem et al. [30], experimental evidence supporting the role of unsteady vortex shedding and flame-vortex interactions in sustaining the combustion instability were provided. The interaction of a premixed flame with the transient vortical structures in a turbulent flow has a profound effect on the flame front [31, 32], governed primarily by the turbulent mixing zone behind the trailing edge of any bluff-body flame holder, and by the recirculation zone immediately behind its base.

As mentioned above in section 2.1, a sinusoidaly varying inlet velocity is used to generate a humming instability phenomenon, which is ascribed to the interaction between flame-front and the trailing vortex pattern of the turbulent shear layer behind the step. In order to understand how the flame interacts with the recirculation zone and flow-field behind the step, images of flame dynamics are produced at certain intervals of time over one cycle of the sinusoidal forcing function.

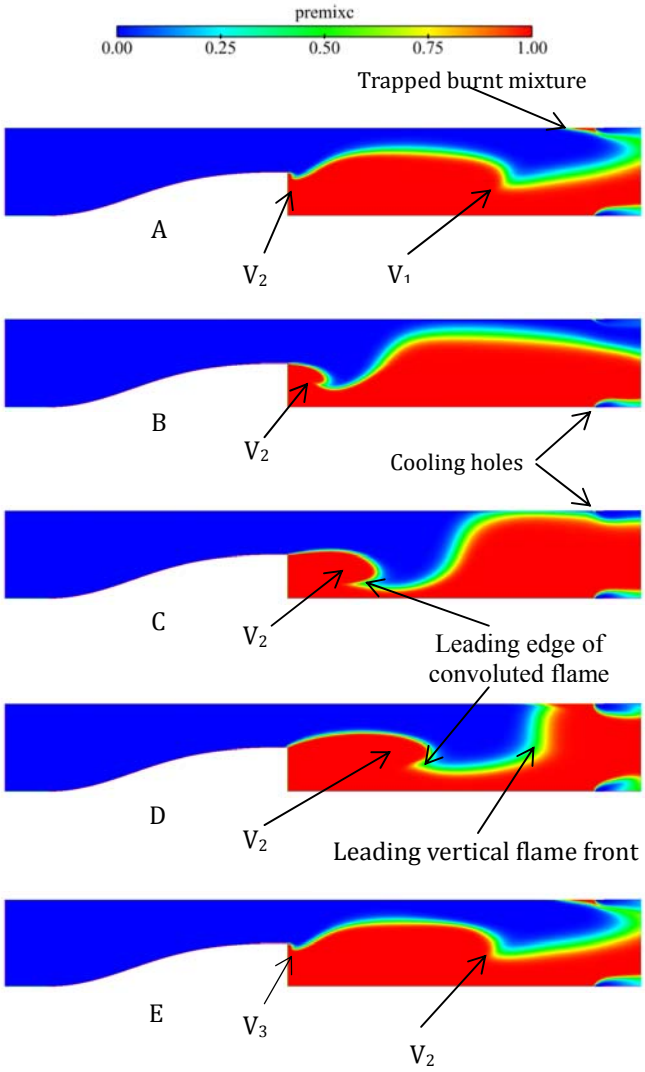

Fig. 7. Pulsed flame front captured by URANS over one excitation cycle (V_{in} = 13.3 m/s, T_{in} = 300 K, Φ = 0.86, excitation amplitude = 50%, frequency = 175 Hz)

Figure 7 shows the images of the high frequency humming cycle captured using URANS at cycle points corresponding to Figure 8. Burnt and unburnt mixture regions in the flow-field downstream of the step are clear to see in Figure 7. The pulsation creates organized structures behind the step. At point A in the cycle, the formation of wake vortex V_2 occurs near the edge of the step, which wrinkles the flame. Downstream, the previous wake vortex V_1 as shown in Figure 7A is moving near the outlet which convolutes the flame around it. Near the upper cooling hole, trapped burnt mixture is seen due to the earlier

interaction between incoming cooling jet and moving flame front.

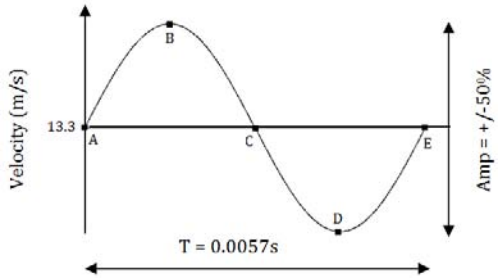

Fig. 8. Inlet velocity sinusoidal forcing function cycle (V_{in} = 13 m/s, T = 0.0057s and Amp = 50%)

As the velocity reaches its maximum at cycle point B, the growing recirculation vortex V_2 of the burned gases causes the previous vortex V_1 (as shown in Figure 7A) to be pushed downstream, while vortex V_2 increases in size. As the flame front convolutes now around vortex V_2, the flame front ahead of the vortex V_2 reaches the wall of the combustor, burning more of the mixture before reaching the outlet. At cycle point C, as the velocity decreases from its maximum value, vortex V_2 continues to grow in size as it moves downstream. The flame advances in to the combustor forming two fronts, a leading vertical front that accelerates forward on the top half of the combustor, and a horizontal front that extends back to the step. Vortex V_2 pushes the unburnt mixture trapped between the convoluted fold of the flame surrounding it and the leading curved flame front moving ahead of it vertically as shown in Figure 7C. At point D, the velocity reaches its minimum value, due to which the flame front is lifted behind the step as vortex V_2 grows and stretches further downstream with its leading edge folded more as compared to cycle point C. Due to the reduced velocity of the mixture; the flame propagates upwards near the wall of the combustor. The leading vertical flame front is pushed further downstream as it reaches the upper wall of the combustor, burning all the mixture leaving the combustor. At cycle point E, the velocity rises again to its original value. A new vortex V_3 is again formed at the step edge with the previous vortex V_2 convecting further downstream. Again, near the upper cooling hole, trapped burnt mixture is observed due to the interaction between the incoming cooling jet and moving flame front. This marks the end of the humming cycle. This process is sustained in a meta-stable mode over a long period of time. The average outlet temperature variation (c.f. Figure 4) is synchronized with this humming cycle.

Figure 9 shows the outlet temperature profile variation at different time intervals of the humming cycle. Each profile corresponds to a cycle point in Figure 8. At point A (start of the humming cycle), most of the mixture escaping from the lower half of the combustor is completely burnt and is at high temperature ~2100 K, whereas, in the upper part, the mixture is mostly partially burned, and at a lower temperature. At cycle point B, due to high velocity, most of the mixture escapes unburnt from the upper part of the combustor which explains the sudden drop in the temperature profile in the upper part.

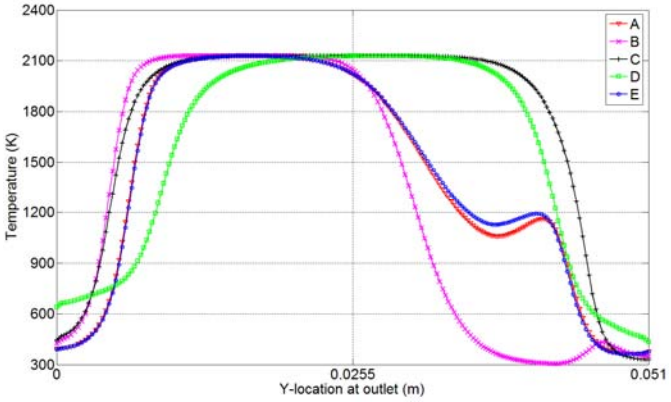

Fig. 9. Outlet temperature profile of the combustor corresponding to humming cycle points (c.f. Figure 8)

At point C, due to the vertically lifted flame front, the incoming mixture is completely burnt before reaching the outlet, hence resulting in a relatively uniform temperature profile at the outlet across the centerline. At cycle point D, the vertical flame front moves forward but due to a lower inlet velocity, the cooling jet bubble flows further away from the combustor wall reducing the amount of burnt mixture leaving the outlet, thus reducing the outlet temperature near the upper and lower walls.

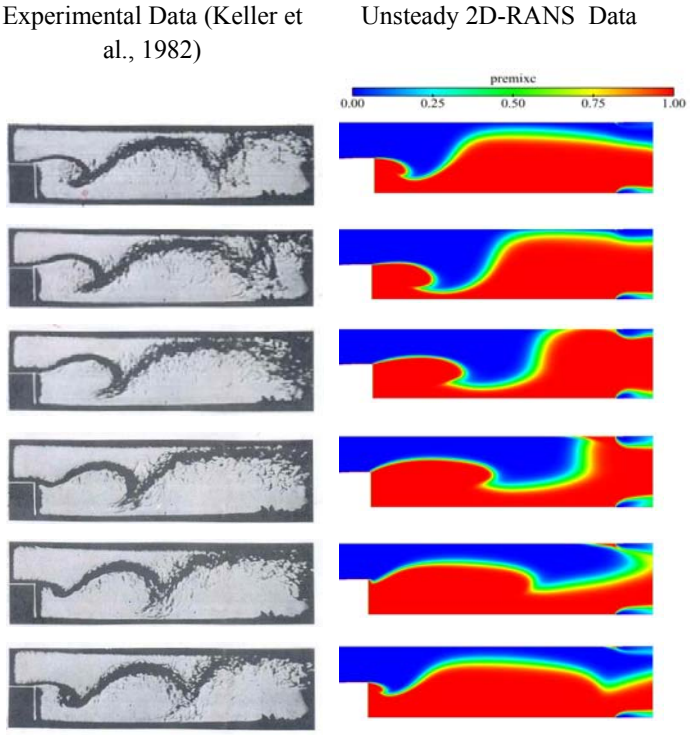

Fig. 10. Humming cycle captured by unsteady RANS in comparison with experimental data of Keller et al. [21] (Time interval between frames: 1ms)

At cycle point E, the inlet velocity increases, pushing the vertical flame front ahead and suppressing the cooling jet bubble flow. The temperature profile for cycle point E matches closely with that of temperature profile at cycle point A.

Figure 10 shows the comparison of the URANS prediction with the experimental data of Keller et al. [22] on the same geometry configuration (c.f. Figure 1). The results are in good agreement, qualitatively, in the near step region where the wake vortex is formed and periodical flame convolution occurs. Away from the step, the flame structure is less accurately captured as the URANS averages instantaneous flame front fluctuations and shows only the mean value. Also, the mesh size used for the reactive URANS simulation is not fine enough to accurately capture the flame front. An appropriate large eddy simulation (LES) on a fine mesh is required in order to capture all details of the flame front propagation and fluctuations, and is not within the scope of the current analysis.

4. OPTIMISATION PROCESS PARAMETERS

4.1 Geometric design and parameterization

The construction of the 2D profiled backward-facing step combustor is carried out using CATIA (Computer Aided Three Dimensional Interactive Application) version V5R18. The flame stabilizer step is constructed and parameterized using an interpolating type cubic spline. The advantages of using a spline are its smoothness and parameterisation properties which allow for control point based shape variation [33].

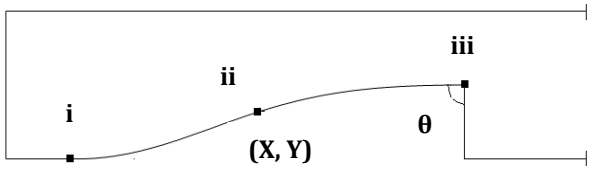

Fig. 11. Flame-stabilizer step design parameterization using spline control points

Figure 11 shows a closer view of the flame stabilizer step (i-ii-iii) baseline geometry. Points i, ii and iii are connected by a spline curve of which control points i and iii are fixed. However, the angle θ at point iii is not fixed. At control point ii, the x-coordinate is fixed at a distance of 95.5mm from the inlet of the chamber and the y-coordinate is variable. Thus, the curve is defined by these two dimensions, namely, Y at control point ii and θ at control point iii. The baseline spline is defined at Y = 17.5 mm and θ = 90 degrees. Thus, two variables [Y and θ] are used to change the shape of the flame-stabilizer step and thus influence the flame/vortex interaction processes downstream.

4.2 Objective function evaluation

Figure 6 shows the outlet temperature profile of the combustor with cooling holes as captured using steady RANS. Much of the mixture that enters the combustor escapes unburnt in the upper half of the combustor behind the step. The objective of the optimisation process is to increase the amount of mixture burning before it leaves through the outlet, thus increasing the combustor's overall efficiency.

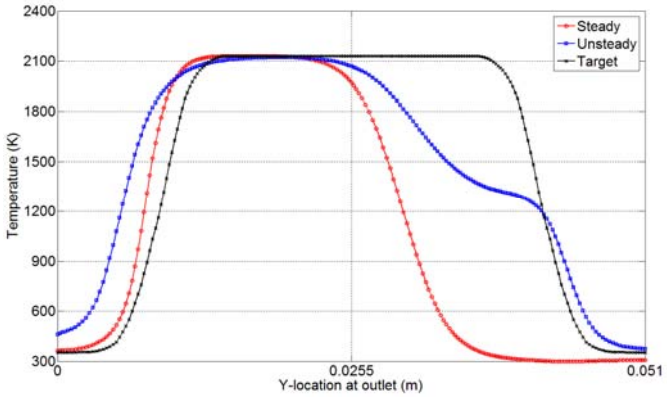

Fig. 12. Comparison between steady RANS and time-averaged unsteady RANS baseline design outlet temperature profile against target outlet temperature profile

Figure 12 shows the comparison between the steady and time-averaged unsteady RANS outlet temperature profile of the baseline flame stabilizer step geometry along with a target outlet temperature profile. The target outlet temperature profile is developed such that it is more symmetrical about the centerline of the combustor, which represents an approximate position of the flame front inside the chamber, above which the mixture is unburnt and below which the mixture is burnt. The aim of the optimization process is to minimize the difference between the design and target profiles as shown in Figure 12. This is done by changing the shape of the flame-stabilizer step i.e. changing the design variables Y and θ (c.f. Figure 11) until a design is found that minimises the root mean square deviation (RMSD) of the difference between the design outlet temperature profile and the target outlet temperature profile. If vector P represents an individual design outlet temperature profile and vector T represents the target outlet temperature profile, then;

For, $T = [T_1, T_2, T_3 \ldots\ldots T_n]$ and $P = [P_1, P_2, P_3 \ldots\ldots P_n]$;

where, n = number of points in the profile;

$$\text{RMSD}\,(T, P) = \sqrt{MSE(T,P)} = \sqrt{\frac{\sum_{i=1}^{n}(T_i - P_i)^2}{n}} \qquad (1)$$

For unsteady RANS, 10 cycles of the inlet velocity sinusoidal fluctuation (5700 time-steps) at a time-step size of 1e-05s are computed. Over the 10th cycle of fluctuation, the outlet

temperature profile is recorded at each time-step, hence recording 570 temperature profiles the cycle.

$$P_i = \frac{\sum P_i^t}{t} \quad \text{, where t = 570} \qquad (2)$$

To calculate the RMSD, all temperature profiles (over the humming cycle) are averaged over the final cycle using Equation 2, and the time-averaged profile is then measured against the target temperature profile using Equation 1.

5. KRIGING BASED DESIGN OPTIMISATION

5.1 Optimisation methodology

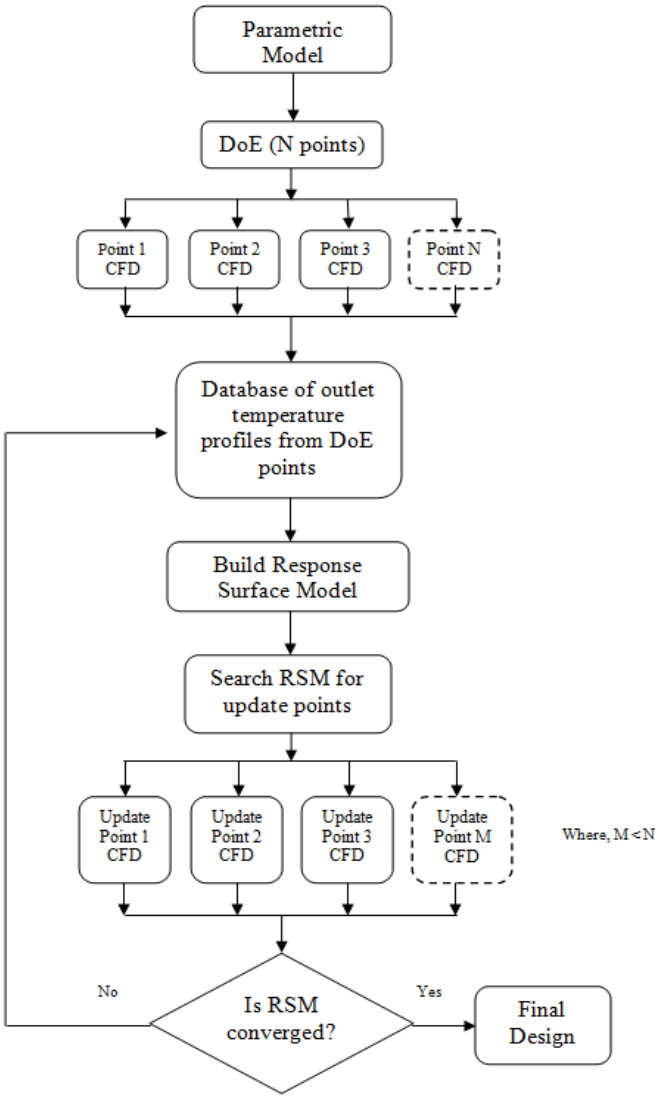

Fig. 13. Optimisation strategy based on Kriging response surface model

Amongst various response surface models (RSM) available such as simple polynomials or radial basis functions, Kriging is the method chosen here for constructing a surrogate model. Besides providing good estimates of complicated landscapes, it also provides an error estimate of the predictor [34]. Kriging, an interpolation method first developed by, and named after, Danie Krige [35], is a set of geostatistical techniques which may be used to estimate unknown values from the data observed at known locations. Introduction to the methodology along with the prediction process is provided by Jones et al. [36] whereas detailed derivation of the method is given by Sacks et al. [37]. Figure 13 shows a traditional Kriging response surface model based design optimisation strategy with N Design of Experiments (DoE) points and M update points per update cycle. Starting with an initial set of 6 Latin Hypercube DoE points, the resulting objective function values are used to construct a Kriging surrogate model. As the surrogate model accuracy is limited due to a relatively small initial sample, the accuracy of the model is increased by adding further update points.

In each update cycle, the surrogate model is searched using a genetic algorithm (GA) followed with a dynamic hill climbing (DHC) algorithm to find a series of three update points per update cycle [38]. For an efficient optimisation strategy, both exploration and exploitation of the design space is necessary in order to search globally interesting configurations and improve the quality of the RSM but at the same time using the already known information to rapidly converge to a global optimum. Hence three update points are found per cycle each using a best predicted criterion, a Kriging prediction error criterion and one using a expected improvement criterion, which in itself is a balanced exploration/exploitation criterion [17]. Three resulting CFD evaluations are then carried out in parallel in each update cycle and the evaluated designs are then added to the existing database of results so as to update the Kriging model. The response surface is re-built and searched again. This process is continued until the RSM is converged or the computational budget gets exhausted.

5.2 Results and discussions

Figure 14 shows the comparison of Kriging RSM captured using a fixed computational budget of 51 CFD runs (six initial points sample and 15 update cycles of three designs each) against a Kriging RSM of 100 CFD runs using a 10x10 regular grid data points, using steady and unsteady RANS computational models. Figure 14(a) and Figure 14(b) shows the Kriging response surfaces for steady RANS analysis. As shown in Figure 14(a), the Kriging surface fits mostly smoothly over the evaluated 10x10 grid of CFD data points indicating a low level of numerical noise in the data. As shown in Figure 14(b), the Kriging based optimisation strategy accurately captures the underlying response and the shape of the surface is closely reproduced after 15 update cycles. It shows a hill of high objective function values at lower design parameter values of Y

and θ, signifying a region of bad designs. The region with good designs consists of a valley surrounding the hill at higher values of Y and θ. Figure 14(c) and Figure 14(d) shows the Kriging response surfaces obtained using the unsteady RANS analysis. As seen in Figure 14(c), the Kriging surface does not fit smoothly over the evaluated 10x10 grid of CFD data points indicating a rather high level of numerical noise in capturing the unsteady humming cycle for different designs of flame-stabilizer step. It shows two basins of potential good designs with a ridge in between created due to a few points which have unreasonably high objective function values pulling up the surface. As shown in Figure 14(d), in this case the underlying response is not well captured using Kriging based optimisation strategy. This is due to existence of high level of noise causing the optimiser to heavily regress the data [39]. It avoids the CFD data points with lower objective function values and constructs the response surface passing through majority of high objective function value data points.

Figure 15 shows the optimisation search histories for the steady and unsteady RANS models using 6 Latin Hypercube DoE runs followed by 45 update point runs. The effect of different initial samples on the optimisation histories is also investigated. Each optimisation is carried out three times, with different random number seeds used to construct the Latin hypercube for the DoE each time. All three optimisation histories along with their mean are plotted in Figure 15. Figure 15(a) shows the optimisation search histories, for the steady RANS model. Figure 15(b) shows the zoomed version of Figure 15(a). As seen in Figure 15(b), different initial DOE's lead to different optimisation search histories as information available at different locations in the design space causes different behaviour in the Kriging response surface model convergence. The search histories for DoE 1, DoE 2 and DoE 3 converge at the 16th, 9th and 21st CFD analysis respectively. However, the DoE 1 search history converges to the best objective function amongst the three.

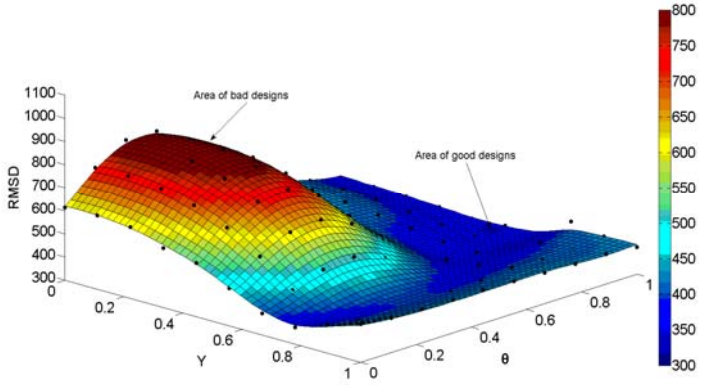

(a) Steady RANS Kriging RSM over 10x10 grid data

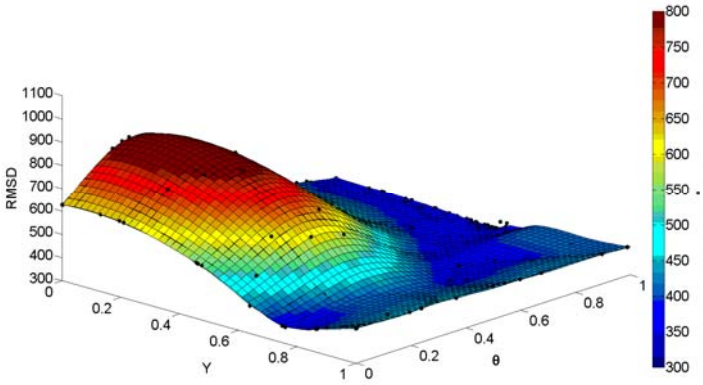

(b) Steady RANS Kriging RSM over fixed budget

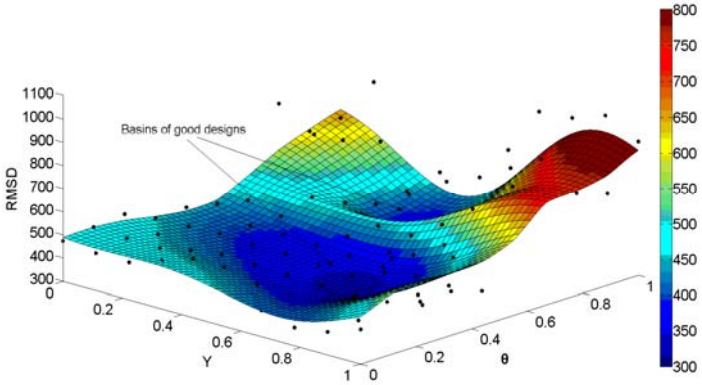

(c) Unsteady RANS Kriging RSM over 10x10 grid data

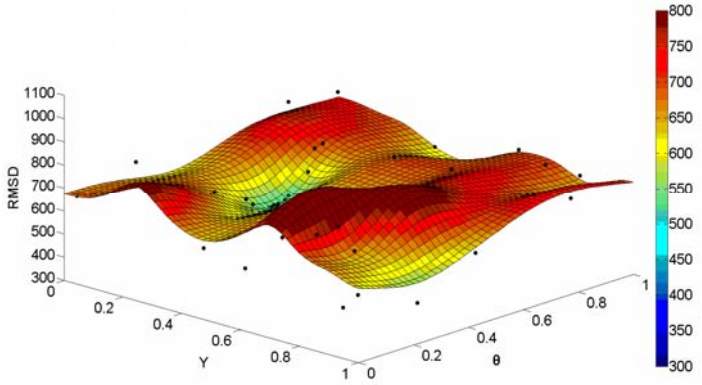

(d) Unsteady RANS Kriging RSM over fixed budget

Fig. 14. Comparison of Kriging RSM captured using fixed computational budget of 6 DoE + 15 update cycle runs against Kriging RSM of 100 CFD runs using a 10x10 regular grid data points

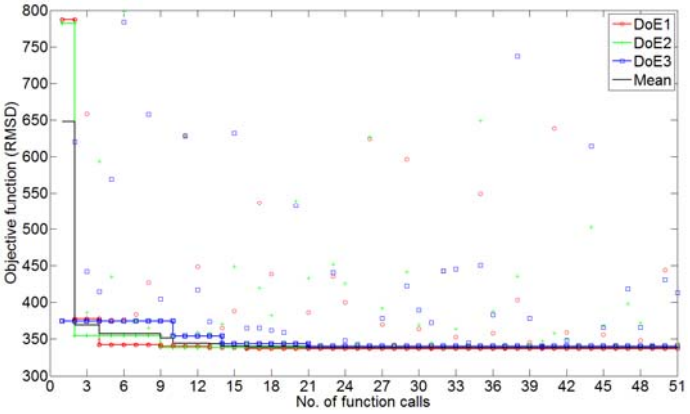

(a) Steady RANS model

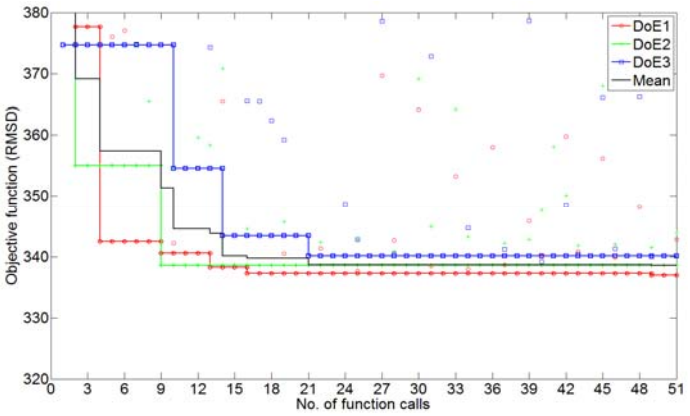

(b) Zoomed image of (a)

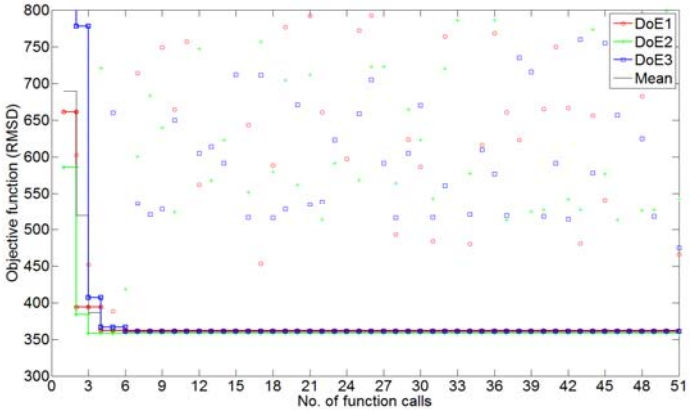

(c) Unsteady RANS model

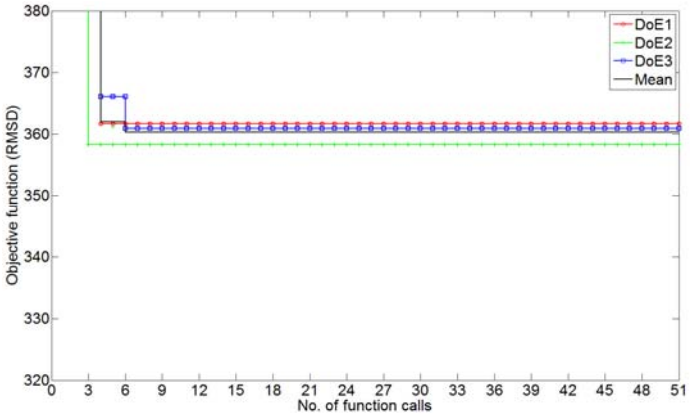

(d) Zoomed image of (c)

Fig. 15. Optimisation search histories over a fixed computational budget of 6 DoE + 15 update cycle (45 update points) runs

The total computational time required for convergence of the mean i.e. for 21 design iterations comprising of 6 DOE runs evaluated in parallel and five update cycle runs (each with 3 update points evaluated in parallel) is approximately 21 hours. Equivalent plots for the unsteady RANS simulations are shown in Figure 15(c). Figure 15(d) shows the zoomed version of Figure 15(c). As seen in Figure 15(d), the Kriging based optimisation strategy is not able to improve on the data obtained from the three initial sample points. Due to the high level of noise in the data capturing the humming cycle (c.f. Figure 14(c)), the Kriging prediction surface is heavily regressed and constructed at higher objective function values, thus avoiding data points with lower objective function values (c.f. Figure 14(d)). All further update points over the next 15 update cycles evaluated by the optimizer lie away from the global optimum, thus indicating a stalled update process. Amongst the three different DoE's DoE 2 leads to the best objective function for the unsteady RANS model. Table 2 summarizes the results of two Kriging based design optimisations (c.f. Figure 15) using steady and unsteady RANS analysis.

Table 2. Details for baseline and optimum designs

Method	Design	Y (mm)	Theta (deg)	RMSD
Steady RANS	Baseline	17.5	90	817.69
	Optimum	25.82	149.9	337.25
Unsteady RANS	Baseline	17.5	90	407.34
	Optimum	20.81	86.1	361.8

6. CO-KRIGING BASED DESIGN OPTIMISATION

6.1 Optimisation methodology

Co-Kriging is an extension to the original form of Kriging [36], which correlates multiple sets of data. CFD simulations can be often run at different levels of complexity, e.g. using two

different levels of mesh resolution, such that there is a relatively accurate but slow analysis along with a fast but inaccurate analysis. However, in the context of design optimisation, these fast approximations, though somewhat inaccurate, may well include important flow-field features and can be used for design search investigation. To improve the efficiency of high-fidelity surrogate based design optimisation systems (c.f. Figure 13), a greater quantity of fast (or cheap) analyses can be used in combination with a smaller number of expensive accurate analyses, in a multi-fidelity co-Kriging methodology, to enhance the accuracy of the high-fidelity function surrogate model at a lower computational cost [40, 41]. Detailed derivation of the co-Kriging model and related discussion can be found in Forrester et al. [17].

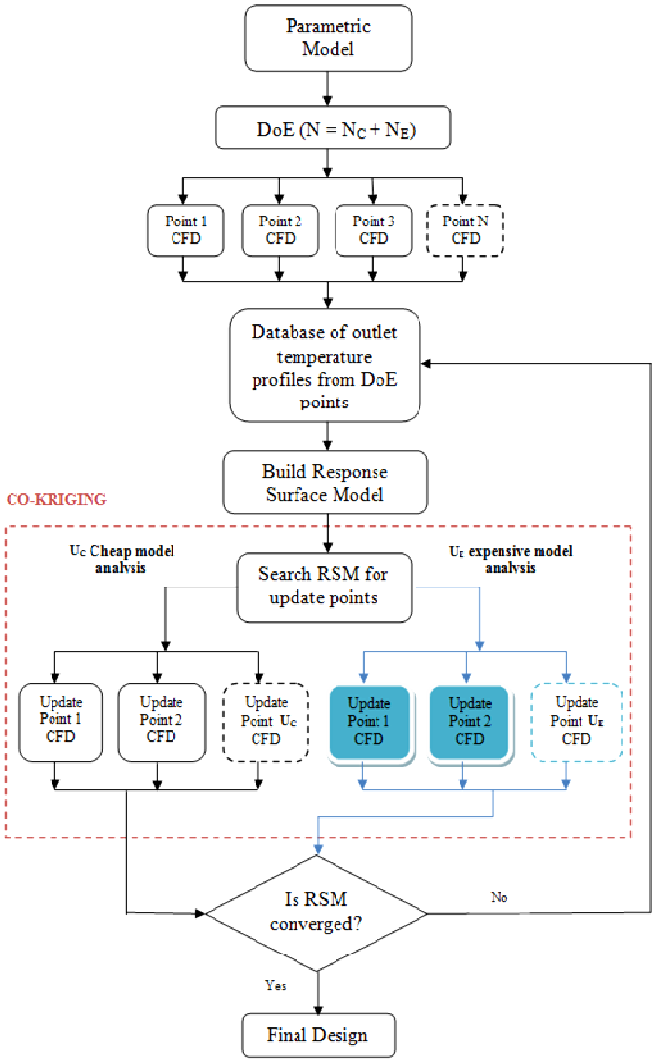

Fig. 16. Optimisation strategy based on co-Kriging response surface model

Figure 16 shows a co-Kriging response surface model based design optimisation strategy with N_C (cheap) and N_E (expensive) DoE points and U_C (cheap) and U_E (expensive) update points per update cycle, where $N_C > N_E$ and $U_C > U_E$. Starting with an initial set of six cheap and three expensive Latin Hypercube DoE points, the resulting objective function values are used to construct a co-Kriging response surface model. The three expensive DoE points are the subsets of six cheap DoE points. To increase the accuracy of the response surface model further update points are selected as mentioned previously in section 5.1. However, out of these three update points, only two expensive update point evaluations are carried out, one using the best predicted point and other using the Kriging prediction error criteria. Hence a ratio of 3 (U_C):2(U_E) is maintained for the 15 update cycle runs. Further investigation of the optimality of this ratio is required.

6.2 Co-Kriging using steady RANS on two grid resolutions

To obtain multi-fidelity data, reactive solutions on two computational grids were obtained using steady RANS analysis. The cheaper low-fidelity data are obtained using a coarse mesh model (mesh 1), consisting of 11000 cells, while the expensive high-fidelity data are obtained using a fine mesh (mesh 3) consisting of 190000 cells.

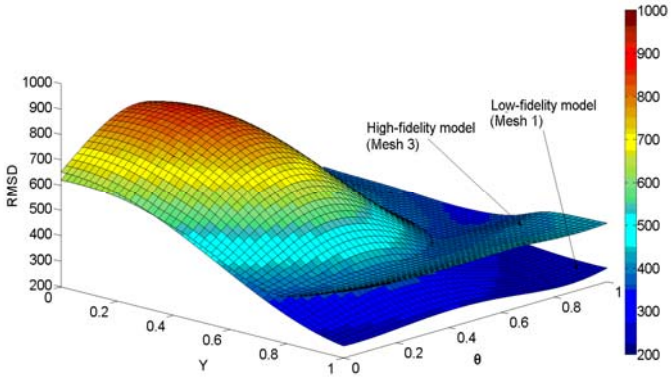

Fig. 17 Kriging response surfaces (overlapped) captured by low-fidelity and high-fidelity models over 10x10 grid data

Figure 17 shows the comparison of Kriging prediction surfaces as captured by low-fidelity and high-fidelity models over a 10x10 grid of CFD data points. The low-fidelity model accurately predicts the response at lower values of Y and θ as compared to the high-fidelity model prediction. However, at higher values of Y and θ, the low-fidelity model under-predicts the value of the objective function relative to the high-fidelity model. The co-Kriging model is then applied to the steady RANS solutions on these two different meshes noting that the RSM's are topologically very similar. As investigated earlier in the Kriging based optimisation strategy, the effect of different initial DoE's on the co-Kriging optimisation search histories is also investigated.

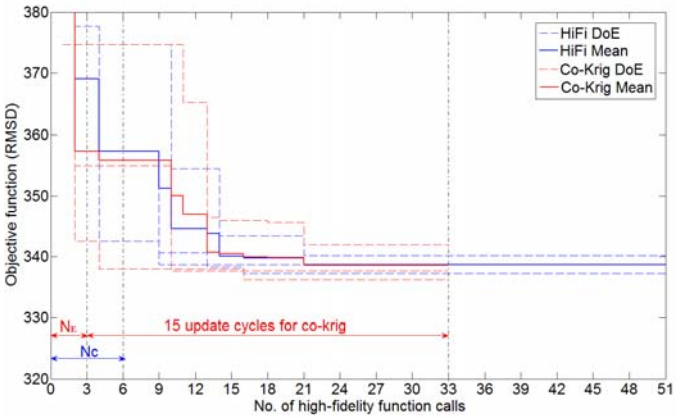

Fig. 18. Kriging and co-Kriging strategies optimisation search histories over a fixed computational budget of DoE + 15 update cycles using three different initial samples

Figure 18 compares the optimisation search histories for the high-fidelity model based Kriging optimisation strategy and the multi-fidelity model based co-Kriging optimisation strategy over a fixed computational budget of 6 DoE points followed with 15 update cycles. The total number of hi-fidelity function evaluations using co-Kriging strategy is 33, whereas using the Kriging based strategy, 51 hi-fidelity function evaluations are carried out. As noted before (c.f. Figure 15a), the mean of the hi-fidelity Kriging strategy converges after 21 hi-fidelity function calls. Here the mean of the co-Kriging strategy also converges after 21 hi-fidelity function calls. However, in addition to the computational time of 21 hi-fidelity function calls during co-Kriging strategy, 24 lo-fidelity function calls have also been carried out. Even though the lo-fidelity model is fast to evaluate, it still adds to the overall computational time. Thus in terms of total computational time, the high-fidelity model based optimisation strategy finds the mean optimum faster, in approximately 21 hours, compared to the co-Kriging based optimisation strategy, which finds the mean optimum in approximately 22 hours. However, the best objective function value design configuration is found by the co-Kriging optimisation strategy using DoE 1. Table 3 summarizes the results of the Kriging and co-Kriging based optimisation strategy using different mesh resolution steady RANS analyses.

Table 3. Details of optimum designs for Kriging and co-Kriging based strategies using steady RANS model

Design	Y(mm)	Theta(deg)	RMSD
Baseline	17.5	90	817.69
Best Kriging	25.82	149.9	337.25
Best co-Kriging	25.43	150	336.21

6.3 Co-Kriging using steady and unsteady RANS solutions

Multi-fidelity data can also be obtained using two different methodologies on the same computational grid. In this method, reactive solutions were obtained using steady and unsteady RANS analyses, both on the same grid (mesh 3). The cheaper low-fidelity data is obtained using the steady RANS model, while the expensive high-fidelity data is obtained using the unsteady RANS model.

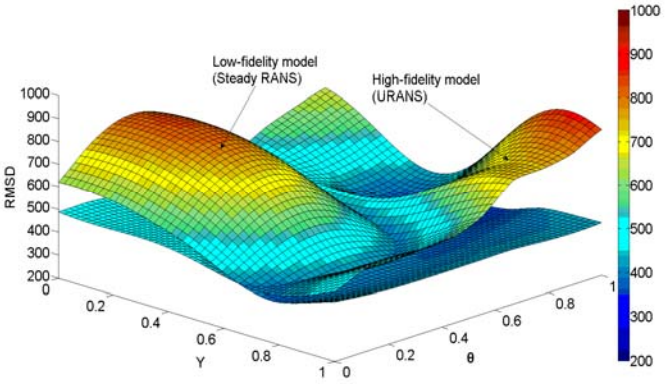

Fig. 19. Kriging response surfaces (overlapped) captured by low-fidelity and high-fidelity models over 10x10 grid data

Figure 19 shows the comparison of the Kriging predictions surface generated for the low-fidelity and high-fidelity models over a 10x10 grid of CFD data points. The low-fidelity and high-fidelity model differ significantly in the landscape orientation and are opposite to each other particularly at lower and higher values of Y and θ. Also, as discussed in section 5, the low-fidelity model response surface is smooth and consists very less computational noise in the data, whereas, the high-fidelity model response surface is heavily regressed as it consists of high level of noise in the data (c.f. Figure 14c). The observed noise in the unsteady RANS data is due to the averaging process of the temperature profile during the unsteady humming cycle and needs a robust filter setup so as to obtain a smoother response.

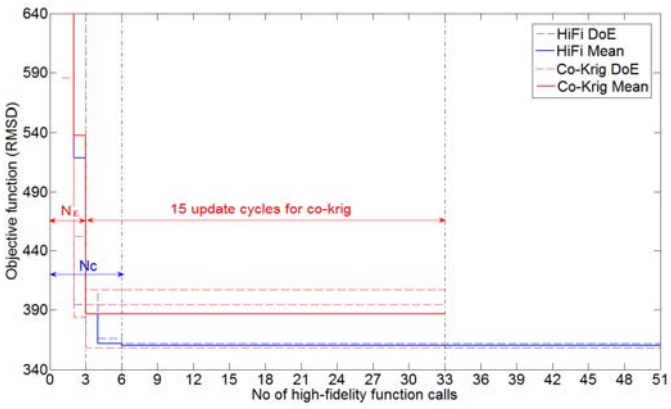

Fig. 20. Kriging and co-Kriging strategies optimisation search histories over a fixed computational budget of DoE + 15 update cycle runs using three different initial samples

Figure 20 shows the optimisation search histories for the high-fidelity and multi-fidelity strategies over a fixed computational budget of 6 initial DoE point followed by 15 update cycles. As seen in Figure 20, the mean of the co-Kriging strategy is above the mean of the Kriging strategy. Both the strategies fail to further improve the best design obtained within the DoE, indicating a stalled update process resulting from a high level of noise in the unsteady simulation data.

7. CONCLUSION

A two-dimensional combustor with a backward facing flame-stabilizer step has been modeled using steady and unsteady RANS formulations. For the steady RANS simulations, a flame-front is established behind the flame-stabilizer step in the region with low mixture velocities. The behaviour is very different in the unsteady RANS case, since an unsteady high frequency humming cycle instability is generated behind the step by imposing a sinusoidal velocity fluctuation at the combustor inlet.

Both the steady and unsteady flow conditions have been studied using Kriging and co-Kriging strategies, constrained by a fixed computational budget. With the steady RANS model, the Kriging prediction captures the shape of the objective function landscape accurately within the given computational budget, whereas with unsteady RANS model, the Kriging prediction fails to capture the shape of the landscape due to a high level of noise in the data which is due the averaging process of the temperature profiles generated during the unsteady humming cycle.

A co-Kriging strategy has been outlined and assessed on two approaches: one using two levels of grid resolutions in a steady RANS formulation and the other using steady and unsteady RANS formulations on the same grid. However, the use of the co-Kriging strategy to correlate sparsely sampled high fidelity data with relatively densely sampled low fidelity data fails to outperform Kriging strategy based on high fidelity data alone, given the same computational budget. Ongoing work is focusing on formulating and applying different co-Kriging strategies and developing a methodology to efficiently filter out the noise and reduce regression in the unsteady CFD Kriging model to obtain more reliable response surfaces.

NOMENCLATURE

$\bar{C}$	: Mean reaction progress variable
$\bar{f}$	: Mean mixture fraction
$\overline{f'^2}$	: Mean mixture fraction variance
Φ	: Equivalence ratio
Ta	: Area-weighted average temperature
Y+	: Dimensionless wall distance
CFD	: Computation Fluid Dynamics
DHC	: Dynamic Hill Climbing
DoE	: Design of Experiments
GA	: Genetic Algorithm
LES	: Large Eddy Simulation
MSE	: Mean Squared Error
RANS	: Reynolds-averaged Navier Stokes
RMSD	: Root Mean Square Deviation
RSM	: Response Surface Model
URANS	: Unsteady Reynolds-averaged Navier Stokes

ACKNOWLEDGEMENT

It is gratefully acknowledged that the work presented in this paper has been supported by Rolls-Royce plc., UK. We are grateful for the input and advice of Dr. Marco Zedda and Mr. Luca Caracciolo, Rolls-Royce plc. and Dr. David Toal, University of Southampton.

REFERENCES

[1] Mongia, H. C., 2001, "A Synopsis of Gas Turbine Combustor Design Methodology Evolution of Last 25 Years," ISABE-2001-1086

[2] Mongia, H. C., 1998, "Aero-Thermal Design and Analysis of Gas Turbine Combustion Systems: Current Status and Future Direction," AIAA Paper No. 98-3982

[3] Nightingale, P., 2000, "The Product-Process-Organization Relationship in Complex Development Projects," Research Policy, Elsevier, Vol. 29, pp. 913-930

[4] Anand, M. S., Priddin, C. H., 2001, "Combustion CFD – A Key Driver to Reducing Development Cost and Time," 15th International Symposium on Air Breathing Engines, Bangalore, India. ISABE-2001-1087

[5] Lefebvre, A.H., 1999, Gas Turbine Combustion, Taylor and Francis, Philadelphia

[6] Wankhede, M. J., Bressloff, N. W., Keane, A. J., Caracciolo, L., Zedda, M., 2010, "An analysis of unstable flow dynamics and flashback mechanism inside a swirl-stabilised lean burn combustor," Proc. ASME Turbo Expo 2010: Power for Land, Sea and Air, GT2010-22253, Glasgow, UK.

[7] Lockwood, F. C., Abbas, T., Kandamby, N. H., Sakthitharan, V., 2000, IJCAT, Computational Reactive Fluid Dynamics: Modelling Software Tools and Applications

[8] Motsamai, O. S., 2008, Optimisation Techniques for Combustor Design, PhD Thesis, University of Pretoria

[9] Epstein, B., Peigin, S., Tsach, S., 2006, "A New Efficient Technology of Aerodynamic Design Based on CFD Driven Optimization," Aerospace Science and Technology, Vol. 10, pp. 100-110

[10] Lighthill, M. J., 1945, "A New Method of Two-Dimensional Aerodynamic Design," Aeronautical

Research Council, London, Rand Report M 2112
[11] Bauer, F., Garabedian, P., Korn, D., Jameson, A., 1975, Supercritical Wing Sections II, Springer Verlag, New York
[12] Hicks, R. M., Henne, P. A., 1978, "Wing Design by Numerical Optimization," Journal of Aircraft, Vol. 15/4, pp. 407-412
[13] Jameson, A., Martinelli, L., Vassberg, J., 2002, "Using Computational Fluid Dynamics for Aerodynamics – A Critical Assessment," In Proc. ICAS 2002, Toronto
[14] Jameson, A., Sriram, Matinelli, L., Haimes, B., 2004, "Aerodynamics Shape Optimisation of Complete Aircraft Configurations Using Unstructured Grids," 42nd AIAA Aerospace Science Meeting and Exhibit, AIAA Paper 2004-0533
[15] Mohammadi, B., 2002, "Optimisation of Aerodynamic and Acoustic Performances of Supersonic Civil Transports," Proc. of the Summer Program, Center for Turbulence Research, Stanford University, CA, pp.285-296
[16] Robinson, T., D., Eldred, M. S., Willcox, K. E., Haimes, R., 2008, "Surrogate-Based Optimization Using Multifidelity Models with Variable Parameterization and Corrected Space Mapping," AIAA Journal, Vol. 46/11, DOI: 10.2514/1.36043
[17] Forrester, A. I. J., Sobester, A., Keane, A. J., 2008, Engineering Design via Surrogate Modelling: A Practical Guide, Wiley, Chichester
[18] Keane, A.J., Nair, P. B., Computational Approaches for Aerospace Design, Wiley, Chichester
[19] Jeong, S., Minemura, Y., Obayashi, S., 2006, "Optimisation of Combustion Chamber for Diesel Engine using Kriging Model," Journal of Fluid Science and Technology, 1(2), 138-146
[20] Duchaine, F., Morel, T., Gicquel, L. Y. M., 2009, "Computational-Fluid-Dynamics-Based Kriging Optimization Tool for Aeronautical Combustion Chambers," AIAA Journal, Vol 47/3 (DOI: 10.2514/1.37808)
[21] Renard, P. H., Thevenin, D., Rolon, J. C., Candel, S., 2000, "Dynamics of flame/vortex interactions," Progress in Energy and Combustion Sciences, pp. 225-282
[22] Keller, J. O., Vaneveld, L., Korschelt, D., Hubbard, G. L., Ghoniem, A. F., Daily, J. W., and Oppenheim, A. K., 1982, "Mechanism of Instabilities in Turbulent Combustion Leading to Flashback," AIAA Journal, Vol. 20, pp.254–262
[23] Najm, H. N., Ghoniem, A. F., 1994, "Coupling Between Vorticity and Pressure Oscillations in Combustion Instability," Journal of Propulsion and Power, Vol. 10/6
[24] Thibaut, D., Candel, S., 1998, "Numerical Study of Unsteady Turbulent Premixed Combustion: Application to Flashback Simulation," Combustion and Flame, Vol. 113, pp. 53-65
[25] User's Guide, 2010, ANSYS FLUENT™ Version 12.1
[26] Poinsot, T., Veynante, D., 2005, Theoretical and Numerical Combustion, Edwards Inc., USA
[27] Poinsot, T. J., Trouve A. C., Veynante, D. P., Candel, S. M., Esposito, E., J., 1987, "Vortex-driven Acoustically Coupled Combustion Instabilities," Journal of Fluid Mechanics, Vol. 177, pp. 265-292
[28] Venkataraman, K. K., Lee, B. J., Preston, L. H., Simons, D. W., Lee, J. G., and Santavicca, D., A., 1999, "Mechanism of Combustion Instability in a Lean Premixed Dump Combustor," Journal of Propulsion and Power, Vol. 15/6, pp. 909–918
[29] Cohen, J. M., Anderson, T., J., 1996, "Experimental Investigation Near Blow Out Instabilities in a Lean Premixed Step Combustor," AIAA 96-0819, 34th Aerospace Sciences Meeting, Reno, NV
[30] Ghoniem, A. F., Annaswamy, A., Park, S., Sobhani, Z. C., 2005, "Stability and Emissions Control Using Air Injection and H2 Addition in Premixed Combustion, Proc. Combustion Institute, Vol 30., pp 1765-1773
[31] Spadaccini, L. J., 1974, "Low Emission Combustors for Gas Turbine Power plants," Combustion Science and Technology, Vol. 9, pp.133-136
[32] Lefebvre, A., H., 1977, "Lean Premixed/Prevaporized Combustion," NASA CP-2016
[33] Weiss, D., 2010, "Feature Based Spline Optimization in CAD: A Step Towards Geometry-Based Structure Creation," Structural Multidisciplinary Optimisation, DOI 10.1007/s00158-010-0521-y
[34] Toal, D. J. J., Bressloff, N. W., Keane, A. J., 2008, "Kriging Hyperparameter Tuning Strategies," AIAA Journal, 46/5, pp. 1240-1252
[35] Krige, D.G., 1951, "A Statistical Approach to Some Basic Mine Valuation Problems on the Witwatersrand," Journal of the Chemical, Metallurgical and Mining Engineering Society of South Africa, 52/6, pp.119-139
[36] Jones, D. R., 2001, "A Taxonomy of Global Optimization Methods Based on Response Surfaces," Journal of Global Optimization, 21/4, pp. 345-383
[37] Sacks, J., Welch, W. J., Mitchell, T. J., Wynn, H., P., 1989, "Design and Analysis of Computer Experiments," Statistical Science, Vol. 4/4, pp. 409-435
[38] Keane, A. J., 2004, OPTIONS Design Exploration System, http://www.soton.ac.uk/~ajk
[39] Forrester, A. I. J., Keane, A., Bressloff, N. W., 2006, "Design and Analysis of Noisy Computer Experiments," AIAA Journal, Vol. 44/10, pp. 2331-2339
[40] Kennedy, M., O'Hagan, A., 2000, "Predicting the Output From a Complex Computer Code When Fast Approximations are Available," Biometrika, 87, pp. 1-13
[41] Forrester, A. I. J., Sobester, A., Keane, A. J., 2007, "Multi-Fidelity Optimization via Surrogate Modelling," Proc. of the Royal Society of London, Series A: Mathematical and Physical Sciences, Vol. 463, pp. 3251-3269, DOI: 10.1098/rspa.2007.1900